SUPPLEMENTARY INFORMATION

The "Pseudo Haber-Bosch" Process for Green Ammonia with Highly Defective and Active Bi_2MoO_6/Cu_8S_5 Electrocatalyst via An Interrupted Chemical Reaction

Abambagade Abera Mitiku[1], Meselu Eskezia Ayalew[1], Tsegaye Girma Eshetu[2], Quoc-Nam Ha[1], Xiaoyun Chen[3], Mikha Zefanya Silitonga[1], Van-Nho Tran[1], Li-Duan Tsai[4], Yin-Wen Tsai[4], Dong-Hau Kuo[1, 2]*

[1]Department of Materials Science and Engineering, National Taiwan University of Science and Technology, Taipei 10607, Taiwan

[2]Graduate Institute of Energy and Sustainability Technology, National Taiwan University of Science and Technology, Taipei 10607, Taiwan

[3]College of Materials Engineering, Fujian Agriculture and Forestry University, Fuzhou 350002, China

[4]Material and Chemical Research Laboratories, Industrial Technology Research Institute, Chutung, Hsinchu 31041, Taiwan

*Corresponding author E-mail: dhkuo@mail.ntust.edu.tw

SUPPLEMENTARY METHODS

1. Experimental Part

1. 1. Chemicals, reagents, and materials

All solutions utilized in the experiments were prepared using distilled water. Reagents were of high-purity grade and employed as received, unless otherwise specified. The following chemicals were used in this work: bismuth (iii) nitrate pentahydrate ($Bi(NO_3)_3.5H_2O$), copper (II) nitrate trihydrate ($Cu(NO_3)_2 \cdot 3H_2O$), and hydrazine monohydrate ($N_2H_4 \cdot H_2O$) from Alfa Aesar, Sodium molybdate dihydrate ($Na_2MoO_4 \cdot 2H_2O$), thioacetamide (C_2H_5NS), urea ($CO(NH_2)_2$), sodium sulfate (Na_2SO_4), para-(dimethylamino) benzaldehyde (p-$C_9H_{11}NO$), and salicylic acid ($C_7H_6O_3$) from Showa Chemical Industry Co. Ltd., $^{15}N_2$ gas (99% isotopic enrichment) supplied by Hefei Ninte Gas Management Co., Ltd., ethanol (CH_3CH_2OH), ammonium fluoride (NH_4F), and ammonium chloride (NH_4Cl) from J. T. Baker, sodium hydroxide (NaOH), sodium citrate dihydrate ($C_6H_5Na_3O_7 \cdot 2H_2O$), sodium hypochlorite solution (NaClO), sodium nitroferricyanide dihydrate ($C_5FeN_6Na_2O \cdot 2H_2O$), hydrochloric acid (HCl), potassium hydroxide (KOH), and Nafion solution from Macklin Ltd, Nessler reagent from MACRO Fine Chemicals, carbon cloth and Nafion membrane was from DuPont Corp.

1. 2. Preparation of nickel foam substrate

Nickel foam (NF) is a highly porous, three-dimensional nickel material commonly used as a conductive support in electrochemical applications. It features a large surface area, remarkable electrical conductivity, reliable mechanical stability, and considerable stability in both alkaline and acidic conditions, making it an ideal catalyst support for reactions such as the electrochemical nitrogen reduction reaction (eNRR). NF was sectioned into pieces (1 × 1 cm^2) from a nickel sheet and immersed in a 3 M HCl solution for 30 minutes to remove surface oxides and impurities [1].

The samples were subsequently rinsed thoroughly in deionized water and anhydrous ethanol to ensure a clean, contaminant-free surface, primarily to remove residual HCl and prevent surface corrosion or chemical interference [2]. The cleaned NF was subsequently vacuum-dried at 80 °C for 2 hours to remove any remaining moisture before use. After drying, the NF was stored in an airtight container to prevent atmospheric contamination.

1. 3. Treatment of carbon cloth substrate

To assess the impact of the NF substrate on eNRR efficiency, the FE and NH_3 yield of the catalyst formed directly on NF were compared with those of the catalyst powder deposited on carbon cloth (CC) using the same experimental setup. For this purpose, CC was cut into 1 × 1 cm^2 pieces and cleaned using $(CH_3)_2CO$, C_2H_5OH, and deionized water to remove surface impurities [3]. After cleaning, CC was soaked in 10% HNO_3 for 30 minutes, rinsed with distilled H_2O, and dried at 60°C for 2 hours to increase its hydrophilicity. The electrocatalyst powder was mixed with a 1000 μL aliquot of Nafion solution (obtained by deionized H_2O, mixing Nafion, and isopropyl alcohol at a volume ratio of 5:1:5 for catalyst ink fabrication). The catalyst ink was then applied to both sides of the CC and oven-dried at 70 °C for 2 hours. Finally, the catalyst powder coated on CC was evaluated for its eNRR performance under identical experimental conditions as the catalyst grown in situ on NF.

1. 4. Electrochemical measurements

Electrochemical studies were conducted in an H-cell using the electrolyte solution of Na_2SO_4 (0.5 M), with a Bio-Logic SP-300 potentiostat employed for data acquisition. A Nafion 211 membrane measuring 3 cm × 3 cm served as a proton (H^+) selective membrane to separate the anode and cathode chambers. The working electrode (WE) consisted of the electrocatalyst synthesized directly on the NF substrate via a one-pot hydrothermal process. A platinum (Pt) film

and Ag/AgCl (sat. KCl) were used as CE (counter electrode) and RE (reference electrode), respectively, for the electrochemical activity measurements.

SUPPLEMENTARY DISCUSSIONS

1. 5. Determinations of NH_3 and N_2H_4

Several analytical methods have been developed to quantify NH_3, including ^1H NMR, ion chromatography, fluorescence spectroscopy, and colorimetric methods [4]. Among these, IPB, Nessler's reagent, and ^1H NMR were used in this study to confirm the formation of NH_3. Results obtained from these techniques were in strong agreement, demonstrating their reliability and accuracy for NH_3 detection.

IPB method

To verify the successful reduction of N_2 and assess the efficiency of the electrochemical process, it is essential to accurately identify and quantify the NH_3 produced following the eNRR. The IPB method, also known as the salicylate method, is one of the most widely employed techniques for NH_3 quantification and was used in this study to spectrophotometrically determine the concentration of NH_3 produced. NH_4Cl standard solutions were prepared at concentrations of 0.0, 0.2, 0.4, 0.6, 0.8, 1.0, 1.2, and 1.4 μmol mL^{-1}, and their absorbance was measured by UV-Vis spectroscopy over the wavelength range of 500-800 nm. Using standard NH_4Cl solutions, a calibration curve was constructed by plotting absorbance versus NH_4Cl concentration to enable quantitative analysis of NH_3. The linear regression analysis yielded the equation $y = 0.68011x + 0.00195$, with a coefficient of correlation (R^2) equal to 0.999, demonstrating a robust linear relationship between absorbance and NH_4Cl concentration. This calibration was validated through three independent trials and subsequently used to quantify NH_3 concentrations in the experimental samples. Over the two-hour timeframe of the eNRR process, 1 mL aliquots of the catholyte were

sampled from the cathode compartment at half-hour intervals and combined with 2 mL (1.0 M NaOH) containing 5 wt.% (salicylic acid) and 5 wt.% (sodium citrate), subsequently adding 1 mL (sodium hypochlorite,0.05 M) and sodium nitroferricyanide dihydrate (0.20 mL, 1 wt.%) [5]. After being kept in the dark at lab temperature for 120 min, the absorbance of the collected samples was measured using UV-Vis over the spectral range of 500-800 nm. The addition of IPB reagents to both the standard NH_4Cl solution and the eNRR-derived sample resulted in a characteristic blue-green coloration, indicating the presence of NH_3. The UV-Vis spectra of NH_4Cl solution and the eNRR sample catalyzed by Bi_2MoO_6/Cu_8S_5 exhibited a sharp peak at 655 nm, further confirming the successful formation of NH_3 [6]. The eNRR-derived NH_3 sample exhibited a steady increase in absorbance at λ_{max} = 655 nm, with the NH_3 yield rising linearly over the 2-hour electrolysis period, indicating continuous and sustained NH_3 production. To assess reproducibility, all measurements were performed three times, and no NH_3 background solutions were used during the tests.

Nessler's method

Quantitative analysis of NH_3 was carried out using the colorimetric Nessler's reagent method, applied to both the standard NH_4Cl solutions and the sample obtained from the eNRR. Nessler's method uses a reagent composed of mercury(II) iodide (HgI_2) or potassium iodide (KI), dissolved in a strongly basic medium, typically sodium hydroxide (NaOH) or potassium hydroxide (KOH) [7]. Standard solutions of NH_4Cl at various concentrations (0.0, 0.2, 0.4, 0.6, 0.8, 1.0, 1.2, and 1.4 μmol mL^{-1}) were prepared to establish a calibration curve for NH_4Cl solution. Following the addition of Nessler's reagent, the absorbance of each solution was determined at 420 nm by UV-Vis spectroscopy [8]. A calibration curve was constructed by plotting absorbance against NH_4Cl concentration using standard solutions to facilitate the quantitative determination of NH_3. The resulting linear regression equation, $y = 0.67664x + 0.00516$, with an R^2 of 0.999, confirms an

excellent linear relationship between absorbance and NH_4Cl concentration. While performing the eNRR for a period of 2 hours, 3 mL aliquots of the electrolyte were sampled from the cathodic chamber every 30 minutes. Each aliquot was mixed with 100 μL of freshly prepared Nessler's reagent, thoroughly shaken, and incubated at ambient temperature in the dark for 20 min to ensure complete color development. Subsequently, the resulting yellow-brown coloration, indicative of NH_3, was analyzed by absorbance at 420 nm using a UV-Vis instrument. The standard NH_4Cl solution and the eNRR sample catalyzed by Bi_2MoO_6/Cu_8S_5 exhibited the same characteristic color upon reaction with Nessler's reagent. The strength of the developed yellow-brown coloration was positively correlated with the concentration of NH_3, as confirmed by the correlation between the absorbance values of standard NH_4Cl solutions and the eNRR-derived NH_3 samples over time. All experiments were performed in triplicate to ensure reproducibility, and no background NH_3 solutions were used to avoid false positives.

Watt-Chrisp method

Hydrazine (N_2H_4), a potential side product of the eNRR, was quantitatively monitored in the cathodic electrolyte using the Watt-Chrisp colorimetric method. To enable the accurate quantification of N_2H_4 in the electrolyte, a series of standard hydrazine monohydrate ($N_2H_4 \cdot H_2O$) solutions with known concentrations was prepared and analyzed using the Watt–Chrisp colorimetric method. Following the reaction with the reagent, the absorbance of each standard sample was recorded at 455 nm by UV-Vis spectroscopy. A calibration curve was constructed by plotting absorbance against $N_2H_4 \cdot H_2O$ concentration, which was subsequently used to determine the N_2H_4 content in experimental samples via interpolation. The coloring reagent for N_2H_4 detection was produced through dissolving 5990 mg of p-$C_9H_{11}NO$ in 3000 μL of HCl (concentrated), with the subsequent addition of 30 mL of C_2H_5OH. During the 2-hour eNRR, 5 mL

aliquots of the electrolyte were withdrawn from the cathodic side every half-hour and added to the prepared coloring reagent (5 mL) for subsequent testing [9]. The resulting mixture was kept in the dark at room temperature for 20 min to ensure complete color formation. Following this period, the sample's absorbance was assessed at 455 nm via a UV-Vis instrument to determine the concentration of N_2H_4 [10]. To evaluate the reproducibility and reliability of the measurements, all experimental procedures were conducted in triplicate under identical conditions. In this study, no detectable hydrazine was observed in any of the samples, indicating that the catalyst exhibits excellent selectivity for the eNRR.

1. 6. Results of Control experiments

Carefully designed control experiments are essential to ensure the accuracy and reliability of eNRR studies. To minimize the risk of residual NH_3 contamination from previous experiments, all components of the H-type electrolytic cell were rigorously cleaned with distilled water before each experimental run. Comprehensive characterization of the as-synthesized catalysts using XRD, XPS, SEM-EDS, and FTIR confirmed the absence of nitrogen in the catalysts, despite the use of nitrogen-containing precursors during synthesis. Recent studies have highlighted multiple sources of potential NH_3 contamination, which can lead to false-positive results in eNRR experiments. These sources include the detection of NO_x compounds (NO_2, N_2O, NO) and NH_3 in the feed gas, membrane, lab equipment-induced surface impurities, electrode, human breath, air, and nitrogen-containing catalyst materials, among others [11]. This observation highlights the importance of conducting rigorous control experiments and providing detailed background quantification to ensure the accuracy of eNRR studies. Such procedures are inherently time-consuming and labor-intensive, but are essential to eliminate false positives and validate actual catalytic activity. The results of these control studies are presented and discussed below.

i. In the Ar-saturated control experiment, where Ar gas was continuously purged throughout the 2-hour electrolysis without introducing N_2 from the feed gas, no detectable NH_3 was observed, confirming that nitrogen reduction did not occur. This result indicates that neither the Ar feed gas, the catalyst, nor any component of the H-type electrolytic cell contributed nitrogenous species. As no external nitrogen source was present, the absence of NH_3 confirms that nitrogen availability is essential for its production, thereby validating that the observed NH_3 in N_2-saturated experiments originates from the eNRR.

ii. During the Ar control experiment, argon gas was continuously purged for 2 hours in the absence of nitrogen gas, and no NH_3 was detected. In contrast, under continuous N_2 purging for 2 hours without Ar, the Bi_2MoO_6/Cu_8S_5 catalyst achieved NH_3 formation rate (3108 μg $h^{-1}cm^{-2}$) and FE (23.8%), confirming its electrocatalytic activity for the eNRR. The detection of NH_3 in the presence of N_2 confirms that N_2 reduction occurred, indicating that the detected NH_3 was derived from the eNRR of the supplied N_2, rather than from background contamination. Furthermore, implementing a pre-treatment step of 30 minutes of Ar purging followed by 30 minutes of N_2 bubbling before the 2-hour eNRR notably enhanced performance, increasing the NH_3 formation rate to 6757 μg $h^{-1}cm^{-2}$ and FE to 57.9%. This significant improvement is primarily attributed to the effective removal of dissolved gases, particularly oxygen, from the electrolyte by Ar gas, thereby promoting a more favorable electrochemical environment for N_2 reduction. Dissolved oxygen can compete with N_2 for electrons and active sites on the catalyst surface, thereby suppressing the eNRR. By eliminating such impurities, the system becomes more conducive to selective N_2 reduction, thereby increasing NH_3

production and improving the electron utilization efficiency. Since Ar gas is denser than air, it effectively displaces oxygen and other gases from confined spaces within the H-type electrolytic cell. Once the impurity gases are removed, the subsequently introduced N_2 gas has greater availability and diffusion space within the system, allowing for improved interaction with the catalyst. This facilitates higher N_2 concentration at the active sites, enhancing the efficiency of the eNRR and promoting greater NH_3 formation. Therefore, applying a 30-minute Ar purging step before eNRR consistently establishes a cleaner, more controlled reaction environment, which is essential for reliable, reproducible, and optimized eNRR performance across all experiments.

iii. To assess potential NH_3 crossover through the Nafion 211 membrane during the eNRR process, electrolyte samples were taken from both cathodic and anodic chambers of the H-cell. The purpose of this experiment was to assess whether NH_3 produced at the cathode could permeate through the membrane into the anodic chamber. Analysis of the sample collected from the anodic chamber revealed no detectable NH_3, confirming that no significant NH_3 migration occurred across the Nafion 211 membrane during electrolysis The Nafion 211 membrane, a proton exchange membrane (PEM), plays a critical role in this system by selectively allowing H^+ transport from the anode to the cathode while maintaining ionic and molecular separation between the two compartments. This physical and chemical selectivity not only facilitates charge balance during the electrochemical reaction but also prevents the back-diffusion of NH_3 and minimizes cross-contamination of reaction products. Such effective

compartmentalization ensures a controlled and reliable environment for accurate evaluation of NH_3 production during the eNRR.

iv. To assess the role of the Nafion 211 membrane in eNRR, an experiment was conducted without the membrane. When the Nafion 211 membrane was not used in the H-type electrolytic cell, only a negligible NH_3 yield was detected. This is attributed to the lack of separation between the cathodic and anodic compartments, which allows for the simultaneous evolution and mixing of N_2, NH_3, H_2, and O_2 within the reactor. Consequently, NH_3 generated at the cathode is susceptible to oxidation at the anode, leading to its loss and underestimation during quantification. Moreover, the dominant HER in aqueous electrolytes can compete with and suppress the eNRR within the same potential window. These factors collectively limit both the NH_3 production rate and FE. The Nafion 211 membrane prevents NH_3 oxidation and cross-contamination, thereby enabling accurate detection and quantification of NH_3 produced solely via N_2 reduction at the cathode.

v. To assess potential interference from atmospheric N_2 or ambient nitrogen-containing species, a control experiment was executed with an unsealed H-type electrolytic cell under open atmospheric conditions. NH_3 was detected at a negligible level after 2 hours of electrolysis in this unsealed H-type electrolytic cell, indicating that contributions from atmospheric nitrogen-containing species are minimal. Although atmospheric N_2 constitutes approximately 78% by volume, its dissolution into the electrolyte is low under ambient pressure in an open system due to the limited solubility of N2 in water. In such configurations, the presence of atmospheric oxygen may further compromise eNRR performance by competing with N_2 for binding at the catalytic active sites and

oxidizing the produced NH_3. This experiment further confirms that the NH_3 detected during the 2-hour eNRR primarily originates from the high-purity N_2 supplied by the gas cylinder, rather than from atmospheric N_2.

vi. To evaluate the possibility of laboratory-derived NH_3 contamination throughout the experiment, a control study was conducted by placing a beaker containing the same volume and composition of electrolyte near the electrochemical workstation, without applying any electrochemical potential. Electrolyte samples were periodically collected and analyzed for NH_3 content using the same detection protocol. Throughout the monitoring period, no detectable NH_3 was detected in the control samples, verifying the absence of external NH_3 contamination. This result validates that the NH_3 detected during eNRR experiments originated from the electrochemical process rather than ambient sources.

vii. To verify that electrochemical processes exclusively drove NH_3 generation, measurements were conducted under open circuit potential (OCP) conditions in N_2-saturated electrolyte. The N_2-saturated electrolyte exhibited no NH_3 formation under OCP, confirming that the presence of N_2 alone is insufficient to induce its reduction in the absence of an applied electrochemical potential. This outcome is consistent with the inherent stability of the N_2 molecule, which possesses a strong triple bond (N≡N, dissociation energy ~941 kJ/mol) and requires substantial energy input to undergo reduction under ambient conditions. This indicates that, without applied bias, the system lacks the driving force needed for eNRR to occur. The eNRR requires an applied potential to overcome the high activation energy of N_2 reduction. Under OCP conditions, no external voltage is applied, so the reaction does not proceed, and no NH_3

is detected. This observation confirms that: (i) the presence of N_2 gas alone is insufficient to drive NH_3 synthesis without an applied electrochemical potential; (ii) necessity of an applied electrochemical driving force to activate N_2 and facilitate its conversion to NH_3, and (iii) any NH_3 potentially generated in previous experiments was not retained or adsorbed on the Nafion membrane surface, or any components of the H-type electrolytic cell.

viii. A single-pot hydrothermal synthesis was employed to grow the electrocatalysts in situ on NF support. To assess the effect of the substrate on catalytic performance, a control experiment was conducted using carbon cloth (CC) as an alternative support. In this setup, the as-prepared catalyst powder was uniformly deposited onto the CC substrate using a thin Nafion film as a binder. The catalyst powder-loaded CC was used as the WE, and the amount of NH_3 produced was quantified and compared with the NH_3 yield obtained from the catalyst grown directly on NF. The amount of NH_3 produced using CC as an alternative support was comparable to that obtained with the catalyst synthesized in situ on NF. This similarity suggests that NH_3 generation predominantly arises from the intrinsic activity of the catalyst's active sites, with minimal catalytic contribution from the substrate. If the NF substrate had played a significant role in enhancing the e-NRR performance, a noticeable difference in NH_3 yield between the NF-supported and CC-supported systems would have been expected. This outcome confirms that NF acts mainly as a conductive support and does not actively participate in the nitrogen reduction reaction. Moreover, the comparable performance between the two conditions suggests that the catalyst's active sites remain equally effective whether the catalyst is directly grown on NF or applied as a powder onto CC. Both NF and CC

likely function as inert, conductive platforms that provide physical support and facilitate efficient electron transport. Additionally, the use of a thin Nafion film as a binder in the CC-based system does not obstruct or deactivate the catalyst's active sites, further affirming that the observed catalytic activity originates from the material itself rather than from the structural or chemical characteristics of the support.

ix. To further assess the influence of the NF substrate on the observed catalytic performance, a control experiment was conducted using bare NF as the WE in an N_2-saturated electrolyte, without any catalyst loading. Under identical electrochemical conditions, only a negligible amount of NH_3 was detected when bare NF was used as the WE. This minimal NH_3 production confirms that NF alone exhibits very limited intrinsic catalytic activity toward the eNRR. Therefore, the observed NH_3 generation from the in situ grown catalyst on NF can be attributed primarily to the intrinsic activity of the Bi_2MoO_6/Cu_8S_5 catalyst, with minimal contribution from the NF substrate itself. The catalyst's active sites primarily facilitate eNRR to NH_3, while the NF serves solely as a conductive support, providing mechanical stability and electrical connectivity. In this context, NF does not contribute directly to the reaction, underscoring the critical role of the Bi_2MoO_6/Cu_8S_5 catalyst in enabling effective nitrogen reduction.

In conclusion, no NH_3 was detected in the absence of the N_2 feed gas, the Bi_2MoO_6/Cu_8S_5 catalyst, or an applied electrochemical potential. These control experiments unequivocally confirm that NH_3 formation originates from the eNRR and is driven by the intrinsic activity of the as-prepared catalyst under the appropriate reaction conditions.

SUPPLEMENTARY TABLES

Table S1. Molar ratios of the as-synthesized catalysts in situ grown on the surface of NF with an exposed area of 1 cm^2.

No	Catalyst label	$Cu(NO_3)_2 \cdot 3H_2O$ mmol	$Bi(NO_3)_3.5H_2O$ mmol	$Na_2MoO_4 \cdot 2H_2O$ mmol	Mass of catalyst (mg)
1	CuBi	3	2	0	2.35
2	CuBi	3	3	0	2.39
3	CuBi	3	4	0	2.41
4	CuBiMo	3	3	1	2.55
5	CuBiMo	3	3	2	2.59
6	CuBiMo	3	3	3	2.62

Table S2. XPS compositional analysis of Bi_2MoO_6/Cu_8S_5 and Bi_2O_3/CuS_2 catalyst.

Catalyst	Element	Peak area (%)		
Bi_2MoO_6/Cu_8S_5	Cu	3.6	Cu^{+}	57.1
			Cu^{2+}	42.9
	Bi	10.4	Bi^{3+}	54.7
			Bi^{5+}	45.3
	Mo	18.3	Mo^{4+}	45.8
			Mo^{6+}	54.2
	S	25.2	S^{2-}	
	O	42.5	O_L	41.7
			O_V	35.8
			O_{OH}	22.5
Bi_2O_3/CuS_2	Cu	20.3	Cu^{+}	56.4
			Cu^{2+}	43.6
	Bi	25.4	Bi^{3+}	-
	S	23.2	S_2^{2-}	44.8
			S^{2-}	55.2
	O	31.1	O_L	41.5
			O_V	34.6
			O_{OH}	23.9

Table S3. Stoichiometric calculation of Bi_2MoO_6/Cu_8S_5 based on EDS and XPS data.

Element	Cu	Bi	Mo	S	O
Molar ratio (**Fig. S2**)	37.31	10.85	5.42	27.29	19.13
Bi_2MoO_6 phase	Elemental analysis of the spherical crystals in **Fig. S3** showed a composition of 30.10% Bi, 15.04% Mo, and 53.05% of O, which is consistent with the data from a broad area (**Fig. S2**). The Bi_2MoO_6 phase can be expressed as: $\left(Bi^{3+}_{0.547}Bi^{5+}_{0.453}\right)_{30.1}\left(Mo^{6+}_{0.542}Mo^{4+}_{0.458}\right)_{15.04}O^{2-}_{53.05}(O_{ad.})_{43.98}$---Charge balance $15.04\left(Bi^{3+}_{0.547}Bi^{5+}_{0.453}\right)_2\left(Mo^{6+}_{0.542}Mo^{4+}_{0.458}\right)_1(O_L,O_{ad.})_6$ In considering the balance of positive and negative defects: $15.04\left(Bi^{3+}_{0.547}Bi^{5+}_{0.453}\right)_2\left(Mo^{6+}_{0.542}Mo^{4+}_{0.458}\right)_1(O_L)_{6-x}$				
Theoretical formula	$Bi_2MoO_6 = Bi_2O_3 \cdot MoO_3$				
Point defect	+	Bi^{2+}_{Bi} : the Bi^{5+}-to-Bi^{3+} defect V^{2+}_{O} : trapped with the adsorbed OH to form $O_{ad.}$			
	−	Mo^{2-}_{Mo} : the Mo^{4+}-to-Mo^{6+} defect			
Cu_8S_5 phase	Elemental analysis of the nanoplate-like structure in **Fig. S4**) revealed 55.66% Cu and 40.93% S, which is consistent with the data from a broad area (**Fig. S2**). The Cu_8S_5 phase can be interpreted as: $\left(Cu^{+}_{0.571}Cu^{2+}_{0.429}\right)_{55.7}\left(S^{2-}\right)_{40.9}$ $8.18\left(Cu^{+}_{0.571}Cu^{2+}_{0.429}\right)_{6.81}\left(S^{2-}\right)_5$ $8.18\left(Cu^{+}_{0.571}Cu^{2+}_{0.429}\right)_{8-x}\left(S^{2-}\right)_5$ ➔ 14.8 % Cu^+ vacancy in all Cu, based upon theoretical formula below.				
Theoretical formula	$Cu_8S_5 = 3\ Cu_2S \cdot 2\ CuS = \left(Cu^{1+}_{0.75}Cu^{2+}_{0.25}\right)_8S_5 = \left(Cu^{1+}_{6}Cu^{2+}_{2}\right)S^{2-}_5$				
Point defect	+	Cu^{1+}_{Cu} : the Cu^{2+}-to-Cu^+ defect			
	−	V^{2-}_{Cu} vacancy, V^{1-}_{Cu} : Cu^+ vacancy			
$5.42\ Bi_2Mo_1O_{6-x} + 5.458\ Cu_{8-y}S_5$ $\sim 50\%\ Bi_2Mo_1O_{6-x} + \sim 50\%\ Cu_{8-y}S_5$					

Table S4. Stoichiometric calculation of Bi_2O_3/CuS_2 based on EDS and XPS data.

<table>
<tr><td>Element</td><td>Cu</td><td>Bi</td><td colspan="2">S</td><td>O</td></tr>
<tr><td rowspan="2">Molar ratio (Fig. S6a)</td><td rowspan="2">13.81</td><td rowspan="2">27.63</td><td colspan="2">27.58</td><td>30.98</td></tr>
<tr><td>12.35 S^{1-}</td><td>15.23 S^{2-}
7.52 for CuS_2</td><td>41.5% O_L= 12.86
58.5% $O_{ad.}$= 18.12</td></tr>
<tr><td>Bi_2O_3 phase</td><td colspan="5">Elemental analysis of the selected region highlighted in the SEM-EDS image (Fig. S6b) revealed a composition of 47.15% Bi and 52.85% O, which is consistent with the data from a broad area. The Bi_2O_3 phase from the broad area SEM-EDS data (Fig. S6a) can be expressed via the charge balance to calculate the anion amount:
$(Bi^{3+})_{27.63}(O^{2-}_{L}\,O^{2-}_{ad.}[OH])_{41.445}$ or 13.81 $Bi_2(O^{2-}_{L}\,O^{2-}_{ad.}[OH])_3$
revealing the chemical formula $^{13.81}\,Bi_2O_{3-x}$.</td></tr>
<tr><td></td><td>–</td><td colspan="4">e’: electrons for n-type semiconductor</td></tr>
<tr><td>Point defect</td><td>+</td><td colspan="4">V^{2+}_{O} : trapped with the adsorbed OH to form $O_{ad.}$ and OH.</td></tr>
<tr><td>CuS_2 phase</td><td colspan="5">Elemental analysis of the region highlighted in the SEM-EDS image (Fig. S6c) revealed an atomic composition of 33.36% Cu and 66.64% S, which is consistent with the data from a broad area. The CuS_2 phase from the broad area SEM-EDS data (Fig. S6a) can be interpreted as
$(Cu^{+}_{0.564}\,Cu^{2+}_{0.436})_{13.81}(S^{-})_{12.20}(S^{2-})_{7.52}$--- Valence charge balance
→ 13.81 $(Cu^{+}_{0.564}\,Cu^{2+}_{0.436})$ $[S^{1-}_{0.883}S^{2-}_{0.545}(V^{1+}_{S})_{0.572}]$ revealing the chemical formula: $CuS_{1.43} = CuS_{2-y}$
Sulfur vacancy has a content of 28.5 % → $[Cu^{1-}_{Cu}] \approx [V^{1+}_{S}]$</td></tr>
<tr><td>Theoretical formula</td><td colspan="5">$CuS_2 = Cu^{2+}(S^{1-})_2$</td></tr>
<tr><td rowspan="2">Point Defect</td><td>+</td><td colspan="4">V^{1+}_{S} : Sulfur vacancy</td></tr>
<tr><td>–</td><td colspan="4">Cu^{1-}_{Cu} : the Cu^{+}-to-Cu^{2+} defect
S^{1-}_{S} : the S^{2-}-to-S^{1-} point defect</td></tr>
<tr><td colspan="6">$^{13.81}\,Bi_2(O,O_{ad.},OH)_3 + {}^{13.81}\,CuS_{2-y}$
$\sim 50\,\%\,Bi_2O_{3-x} + \sim 50\,\%\,CuS_{2-y}$</td></tr>
</table>

Table S5. Comparison of e-NRR performance of as-prepared catalysts (2 h data)

NO	Catalyst code	Cu precursor (mmol)	Bi precursor (mmol)	Mo precursor (mmol)	NH_3 yield rate μg $h^{-1}cm^{-2}$	FE (%)
1	CuMo (3:2)	3		2	2168	18.2
2	BiMo (3:2)		3	2	2513	22.4
3	CuBi (3:2)	3	2	0	2816	24.3
4	CuBi (3:3)	3	3	0	3374	28.9
5	CuBi (3:4)	3	4	0	2914	25.2
6	CuBiMo (3:3:1)	3	3	1	6147	52.8
7	CuBiMo (3:3:2)	3	3	2	6757	57.9
8	CuBiMo (3:3:3)	3	3	3	6300	54.4

SUPPLEMENTARY FIGURES

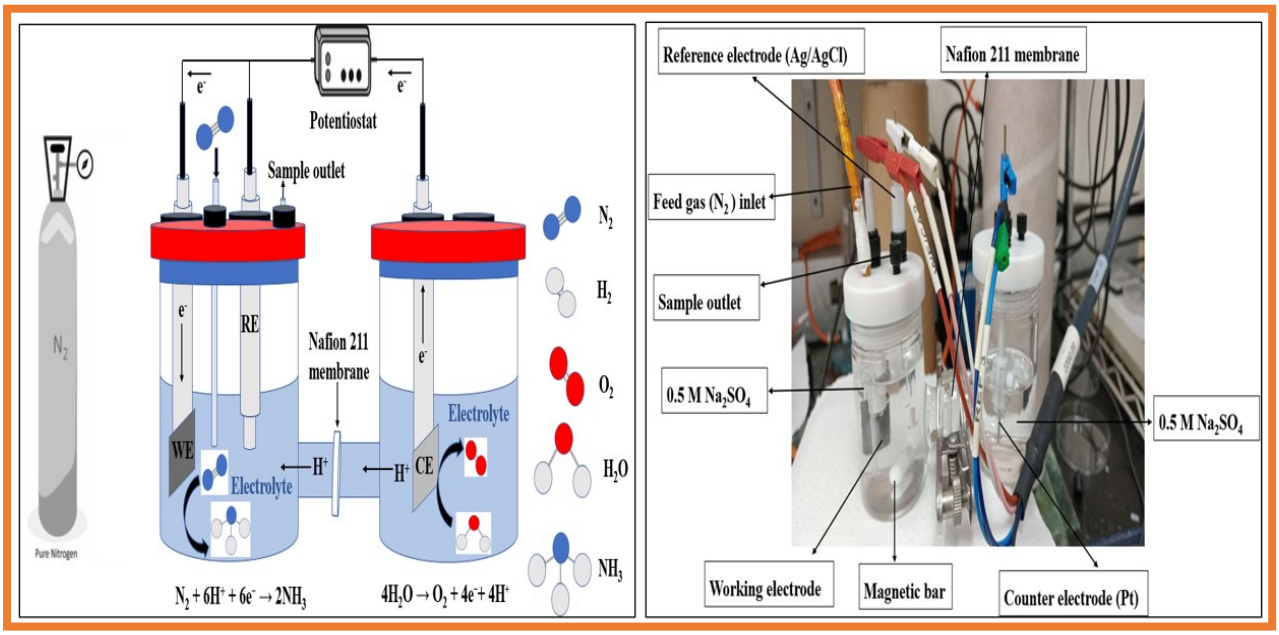

Fig. S1. Schematic illustration and photographic image of H-type electrolytic cell used for eNRR.

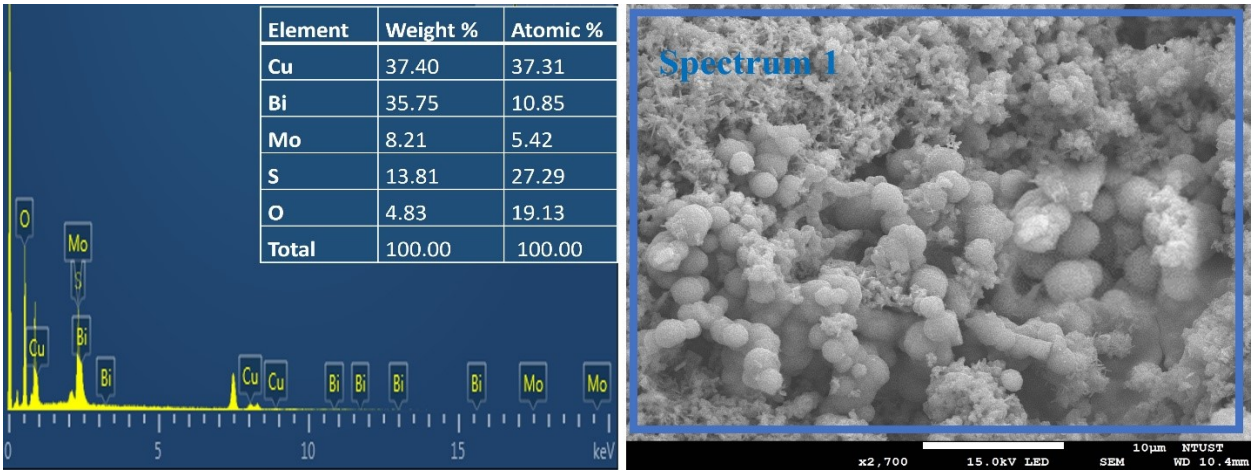

Fig. S2. Large-area EDS spectrum of Bi_2MoO_6/Cu_8S_5 alongside SEM image.

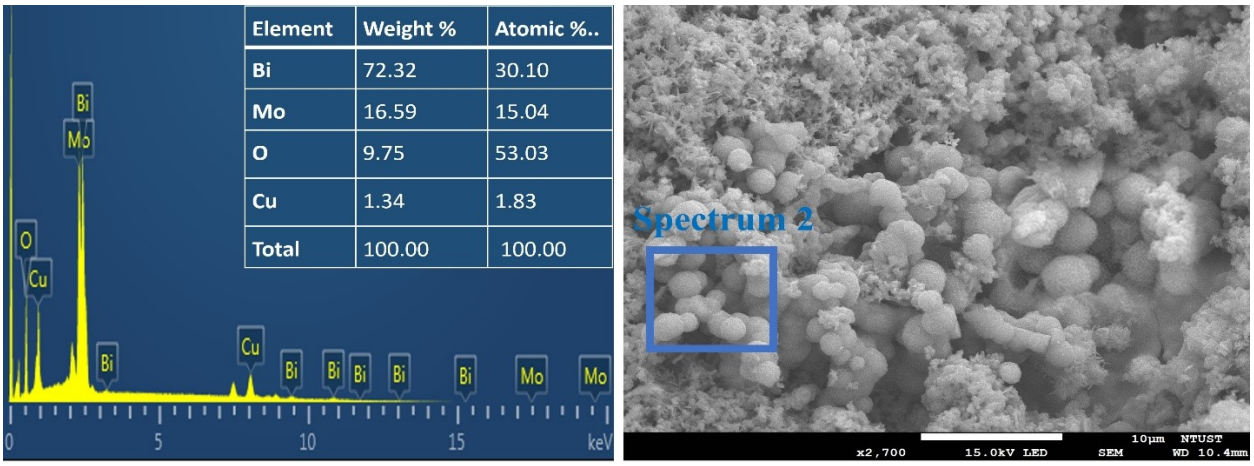

Fig. S3. Selected-area EDS spectrum of Bi_2MoO_6/Cu_8S_5 alongside SEM image.

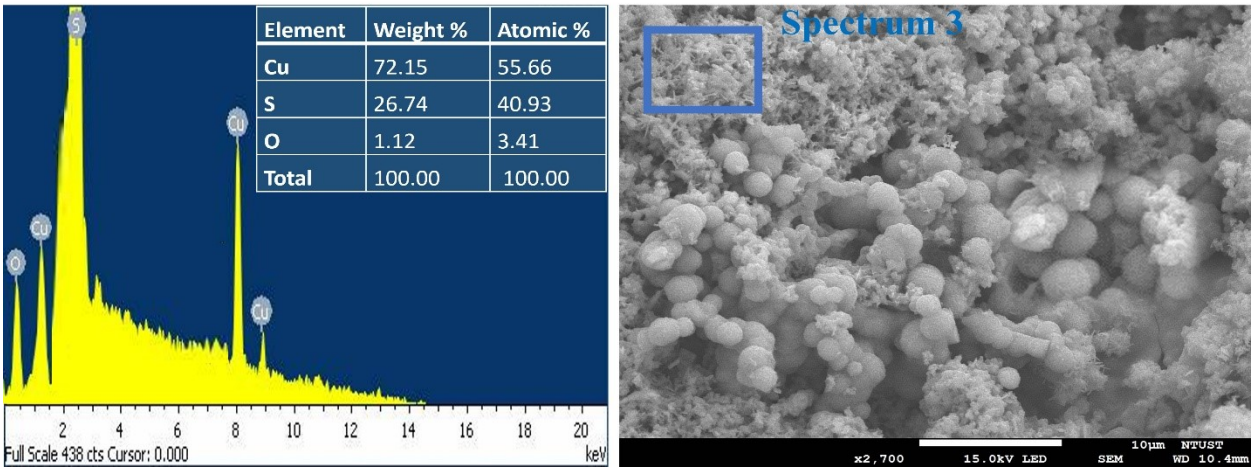

Fig. S4. Selected-area EDS spectrum of Bi_2MoO_6/Cu_8S_5 with its SEM image.

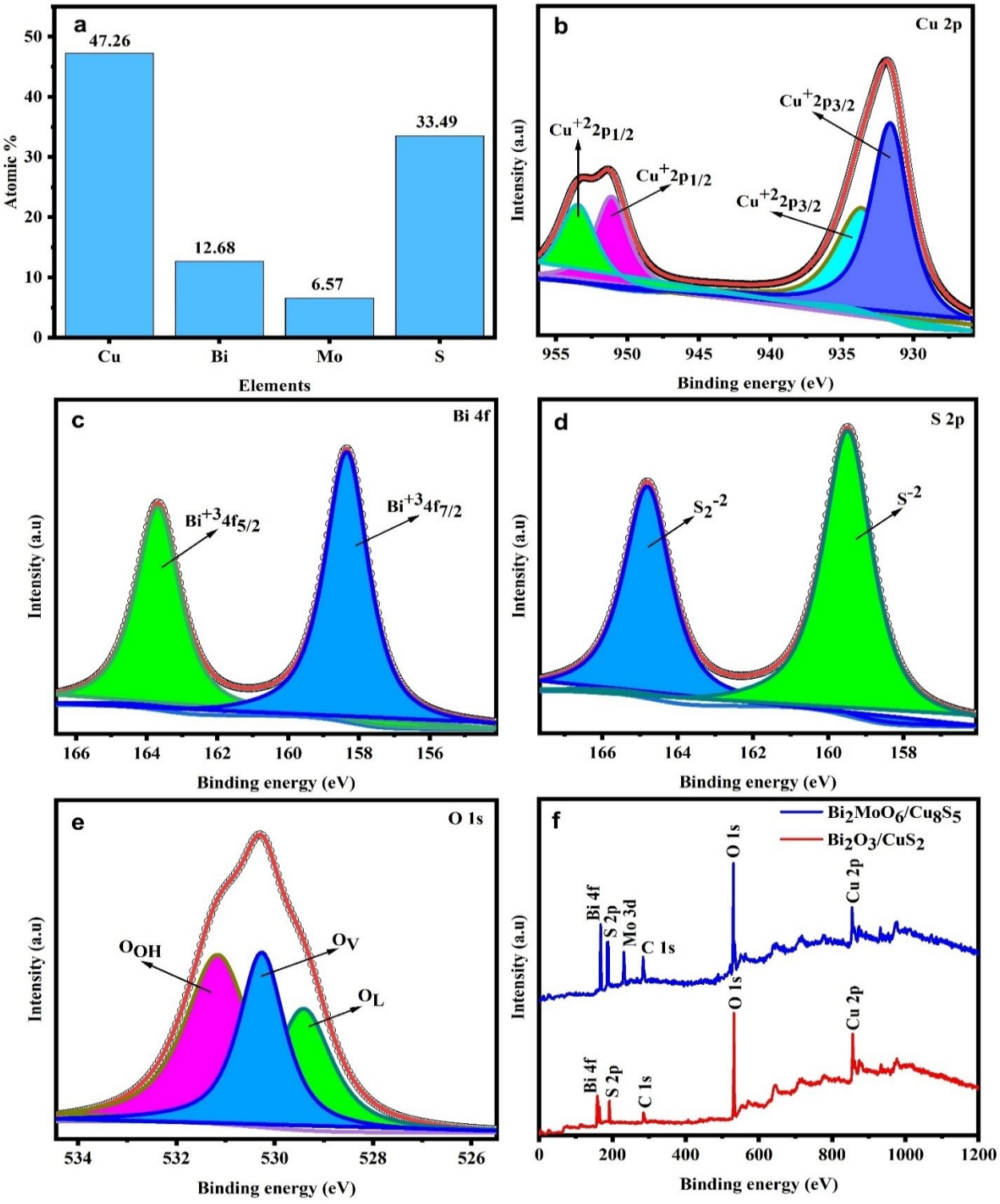

Fig. S5. (a) ICP-MS elemental analysis of the Bi_2MoO_6/Cu_8S_5 catalyst. XPS spectra of CuBi (3:3) for (b) Cu, (c) Bi, (d) S, and (e) O. (f) Comparative XPS spectra for CuBi (3:3) and CuBiMo (3:3:2).

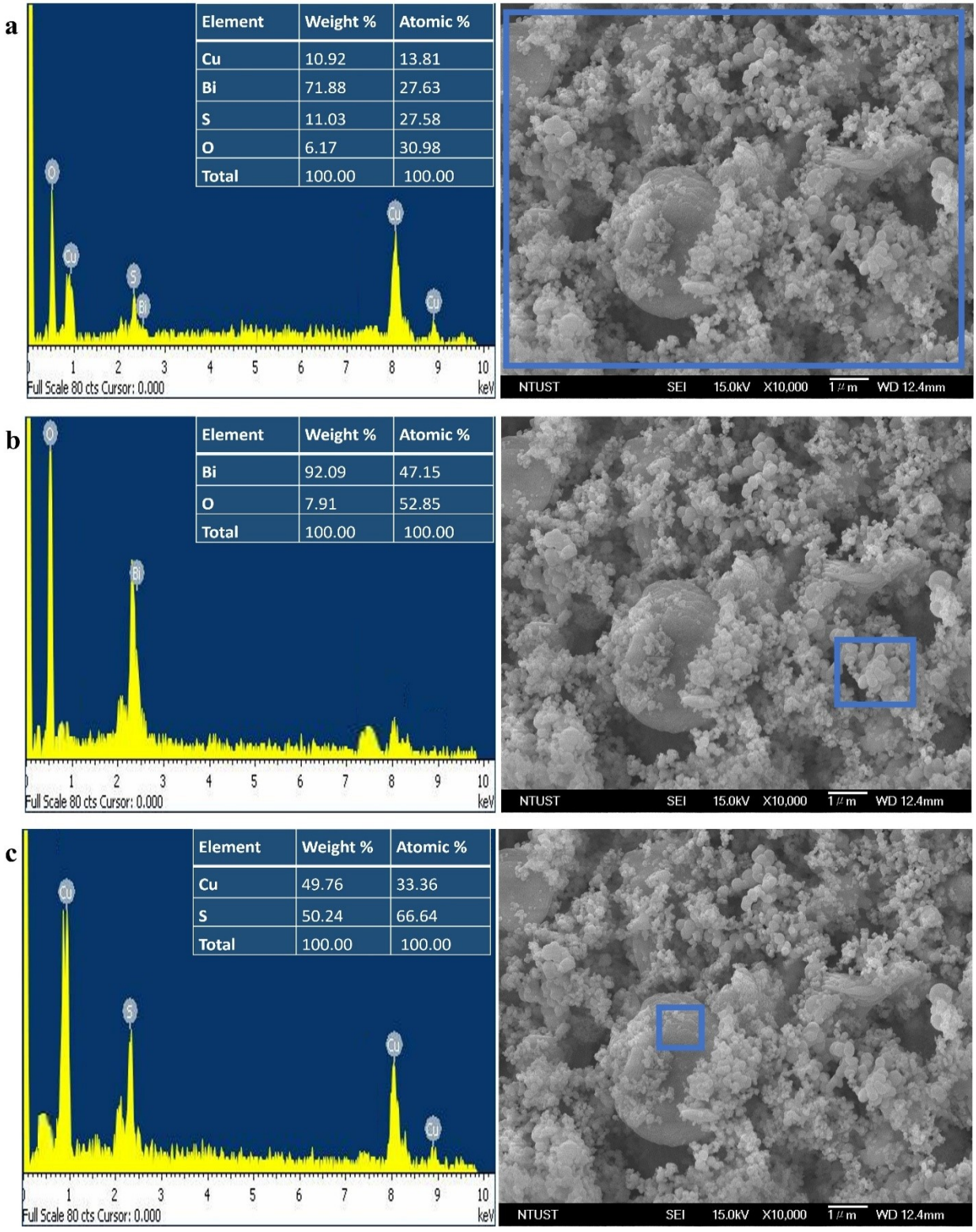

Fig. S6. SEM Morphology and EDS spectra of Bi_2O_3/CuS_2: (a) Large-area and (b, c) Selected-area view.

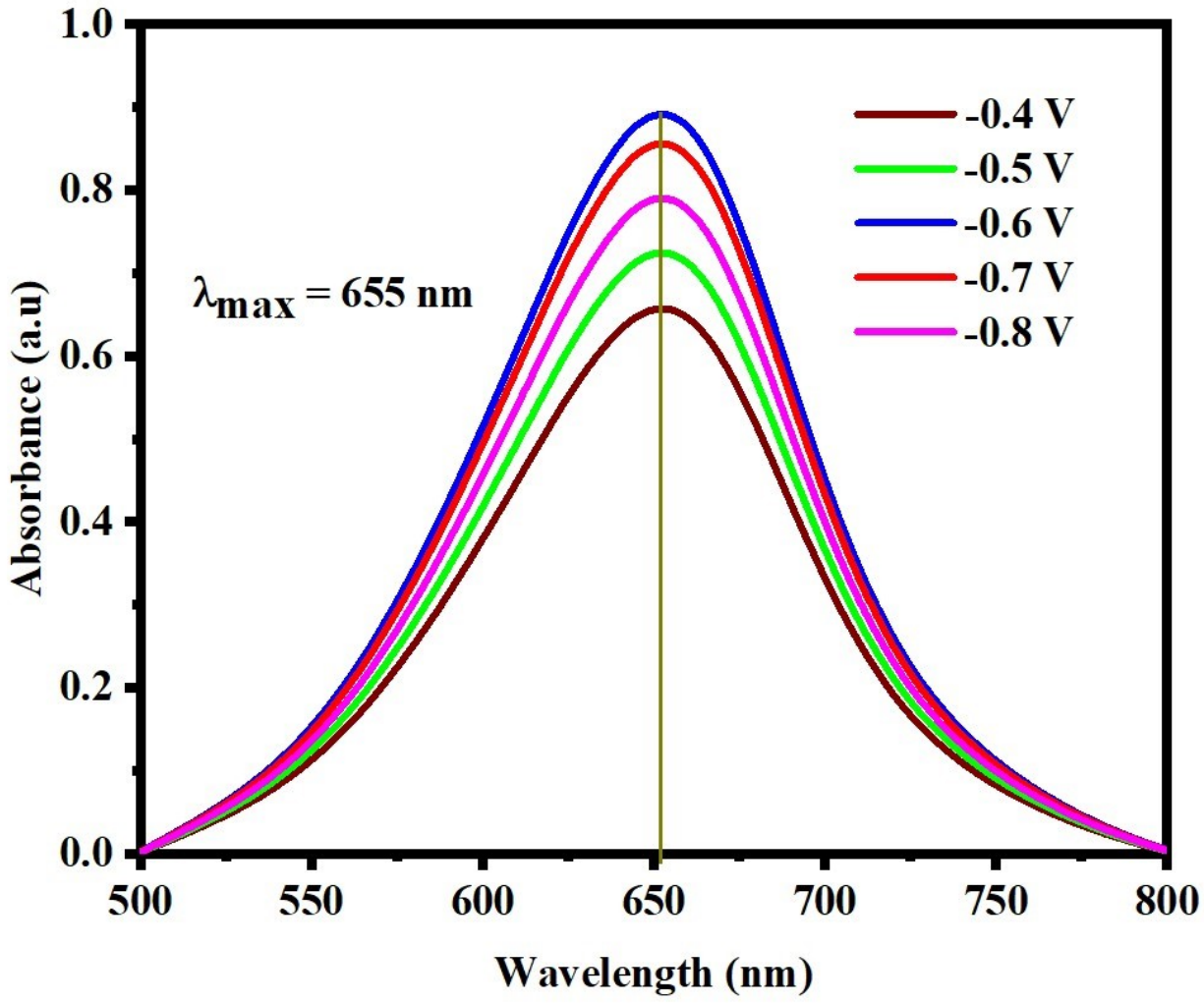

Fig. S7. UV-Vis absorption spectra of the sample after 2 h of eNRR electrolysis at different applied potentials, obtained using IPB.

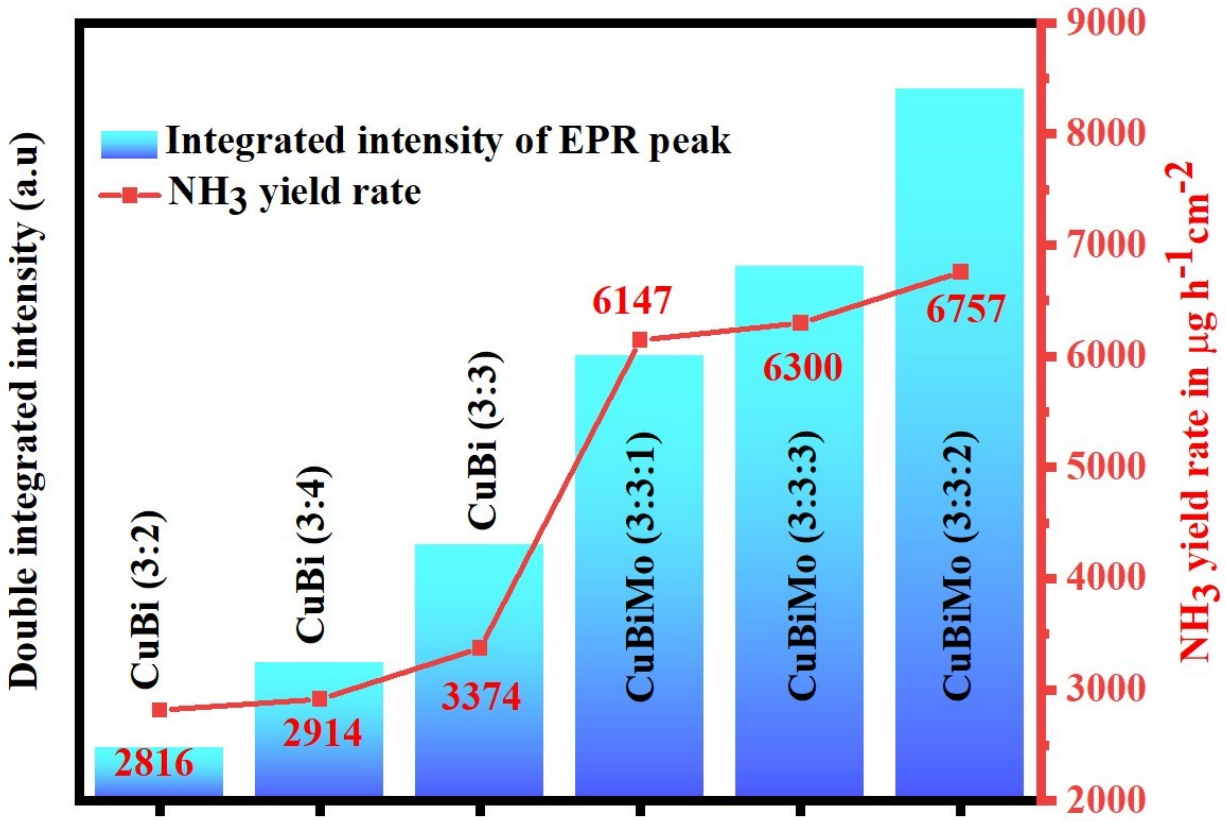

Fig. S8. Correlation between EPR double integrated intensity of O_V and NH_3 yield rate of as-prepared catalysts.

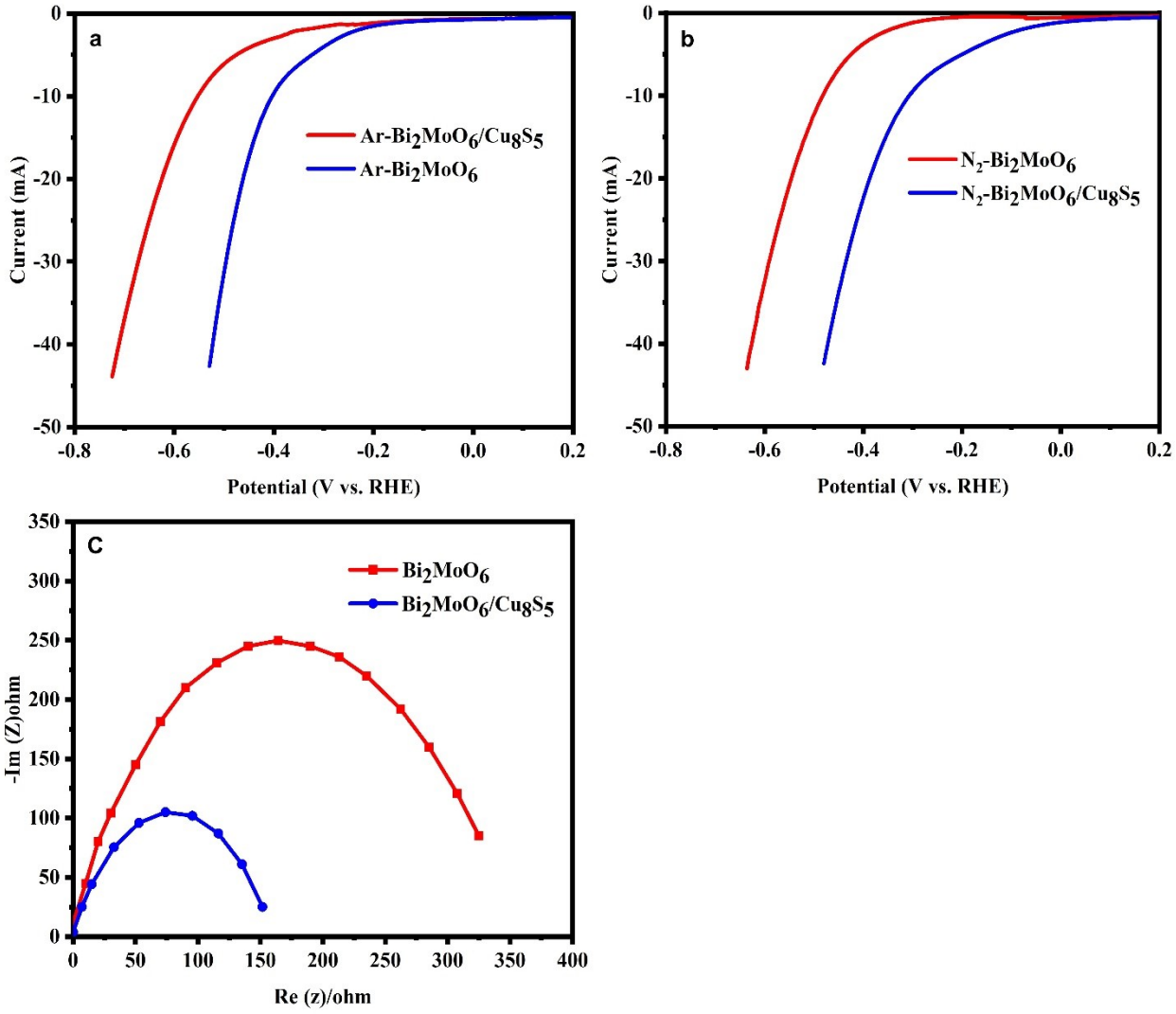

Fig. S9. LSV comparison curves of pure Bi_2MoO_6 and Bi_2MoO_6/Cu_8S_5 under (a) an Ar-filled electrolyte and (b) an N_2-saturated electrolyte. (c) Nyquist plots of electrochemical impedance spectra (EIS) of pure Bi_2MoO_6 and Bi_2MoO_6/Cu_8S_5 composite.

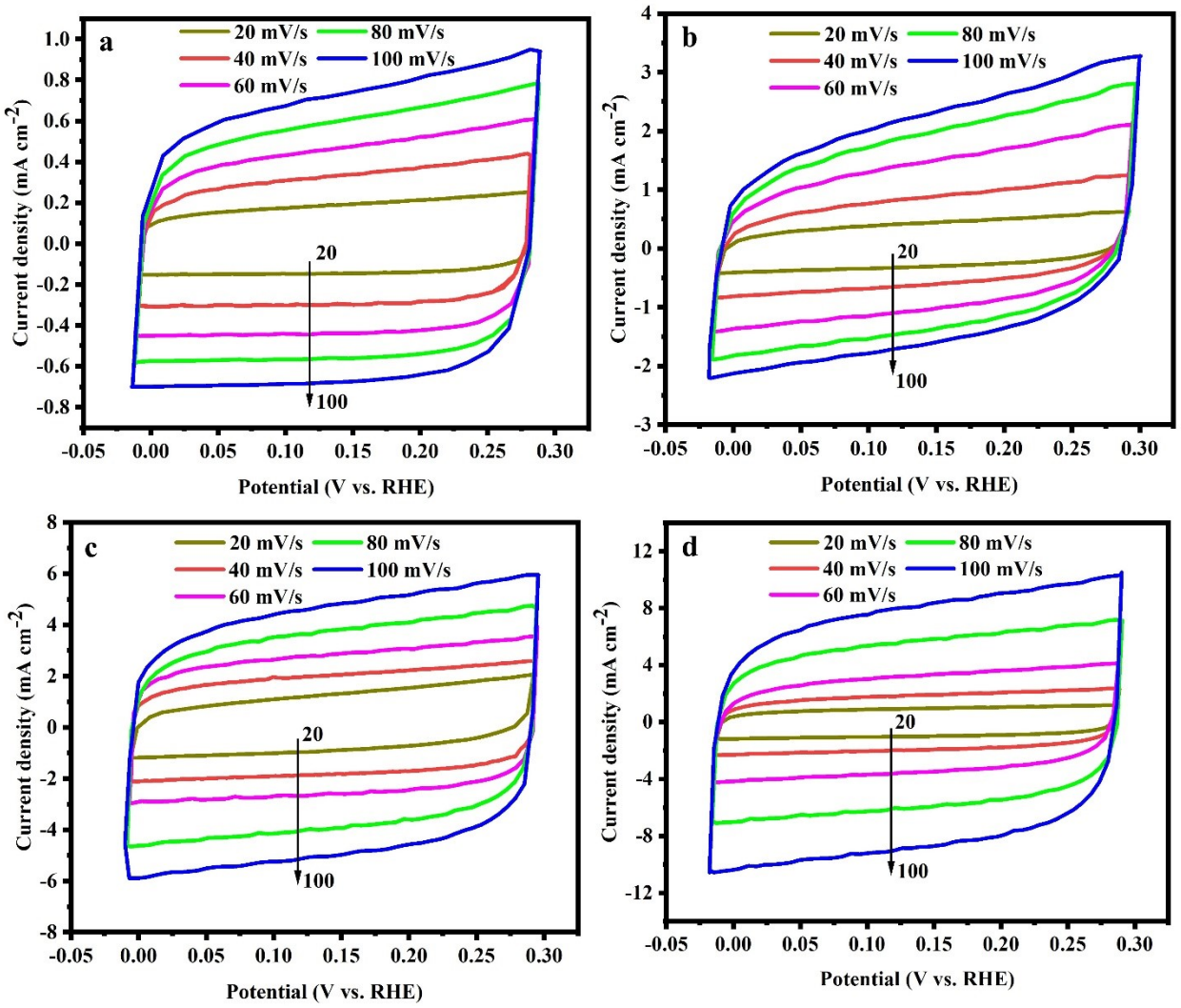

Fig. S10. CV profiles in the non-faradaic region under varying scan rates for (a) CuBi (3:3), (b) CuBiMo (3:3:1), (c) CuBiMo (3:3:3), and (d) CuBiMo (3:3:2).

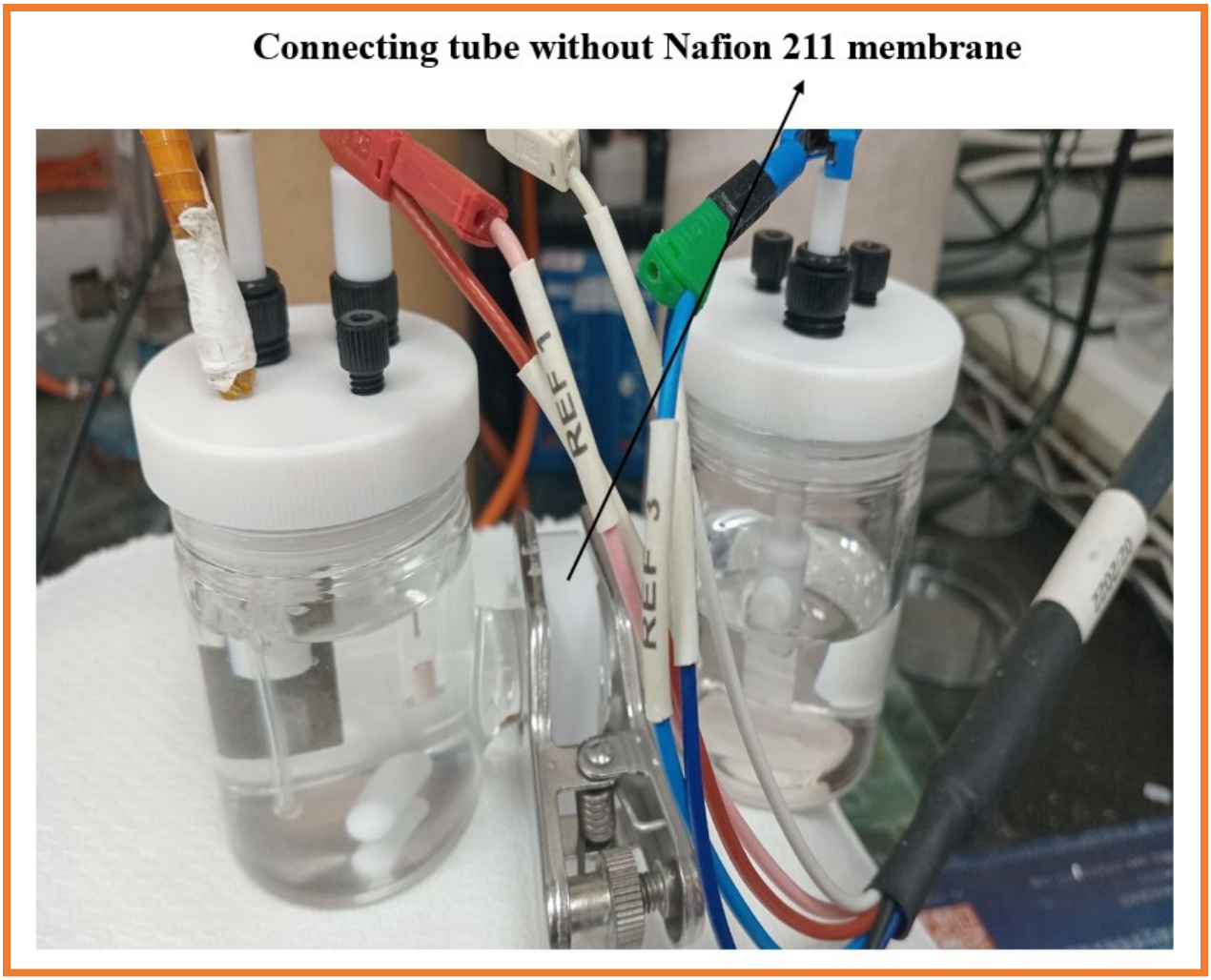

Fig. S11. Image of an H-type cell without the Nafion 211 membrane used in the control experiment.

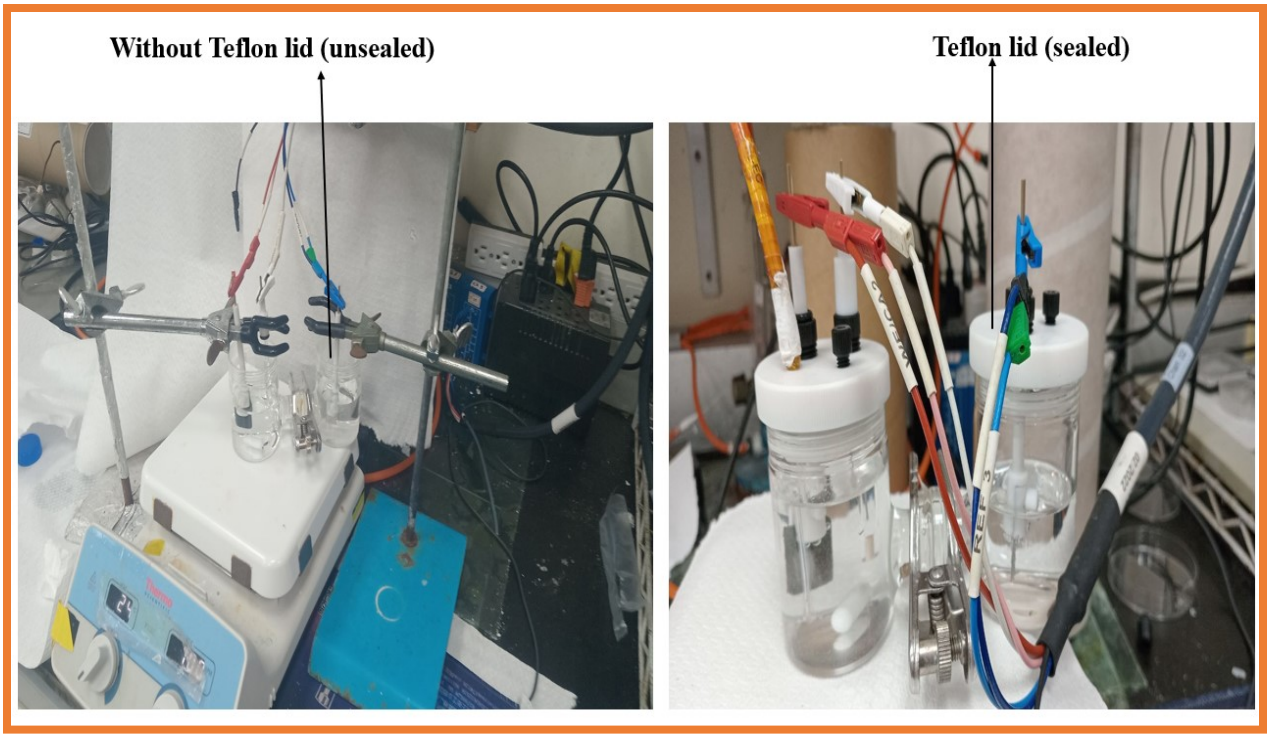

Fig. S12. H-type cell setup during control experiment: unsealed and sealed (with Teflon lid) configurations.

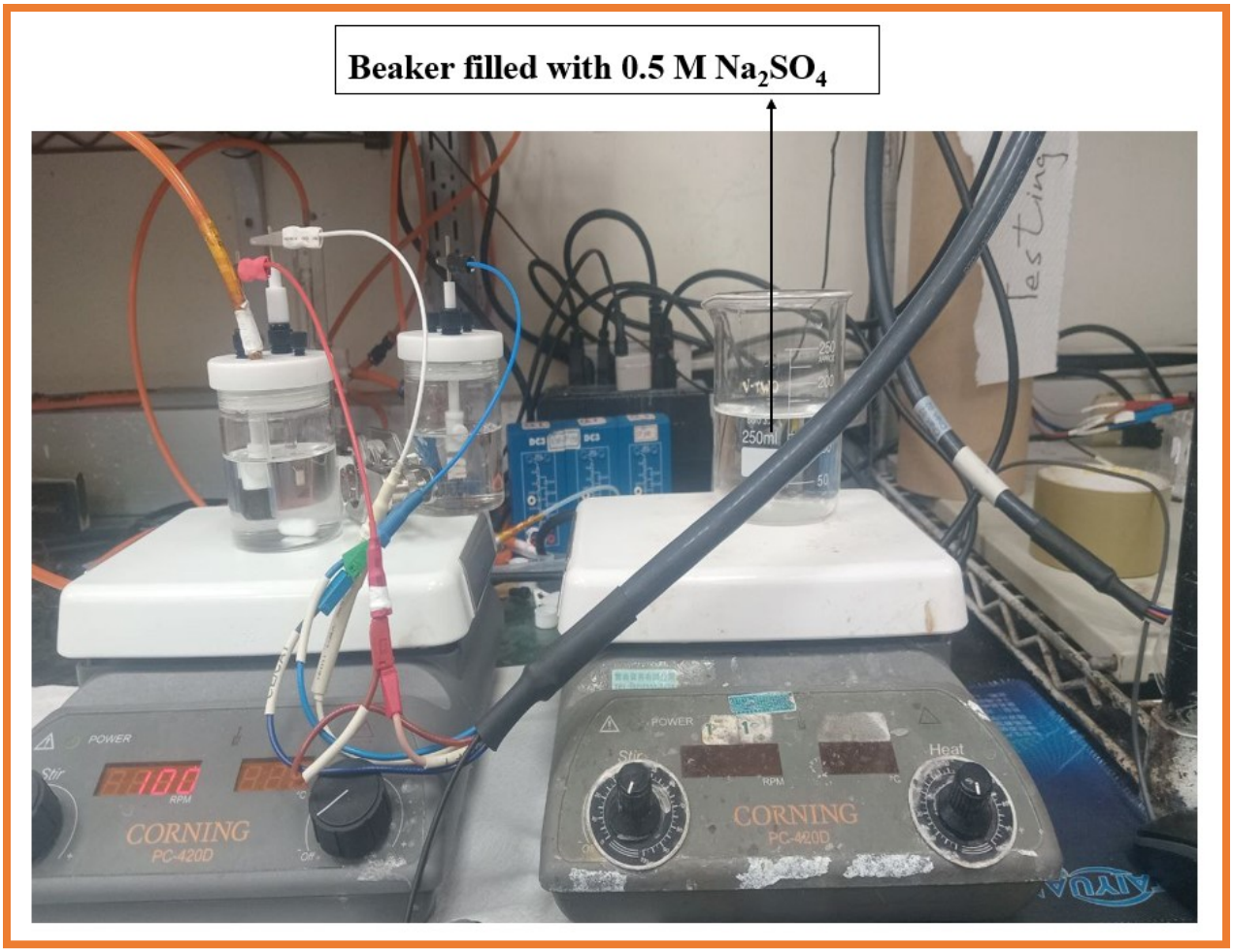

Fig. S13. Image showing a beaker with 0.5 M Na_2SO_4 solution next to the electrochemical workstation during the control test.

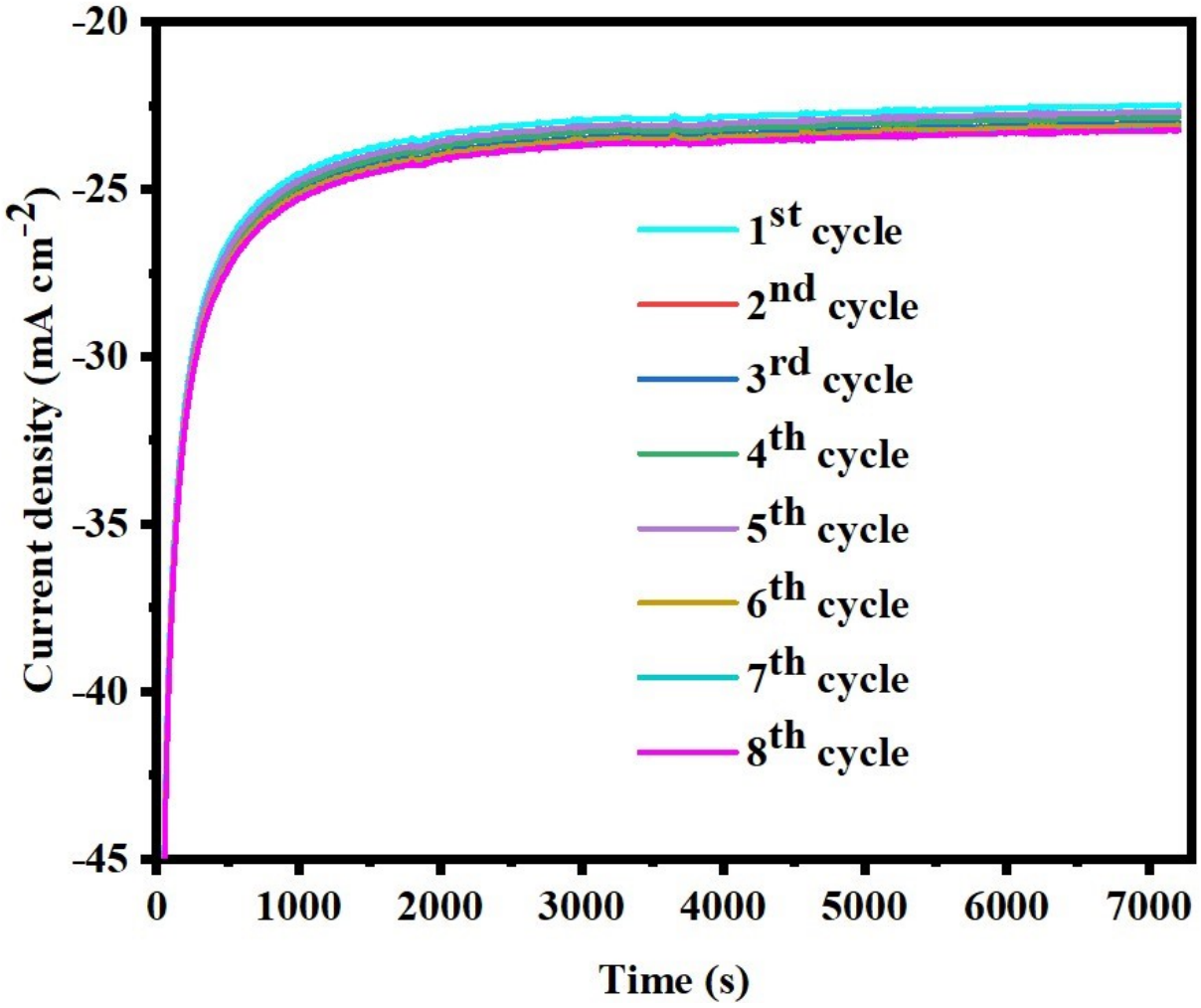

Fig. S14. Eight-cycle CA profiles of the Bi_2MoO_6/Cu_8S_5 catalyst in electrolyte, measured at –0.6 V (vs. RHE) under N_2 saturation.

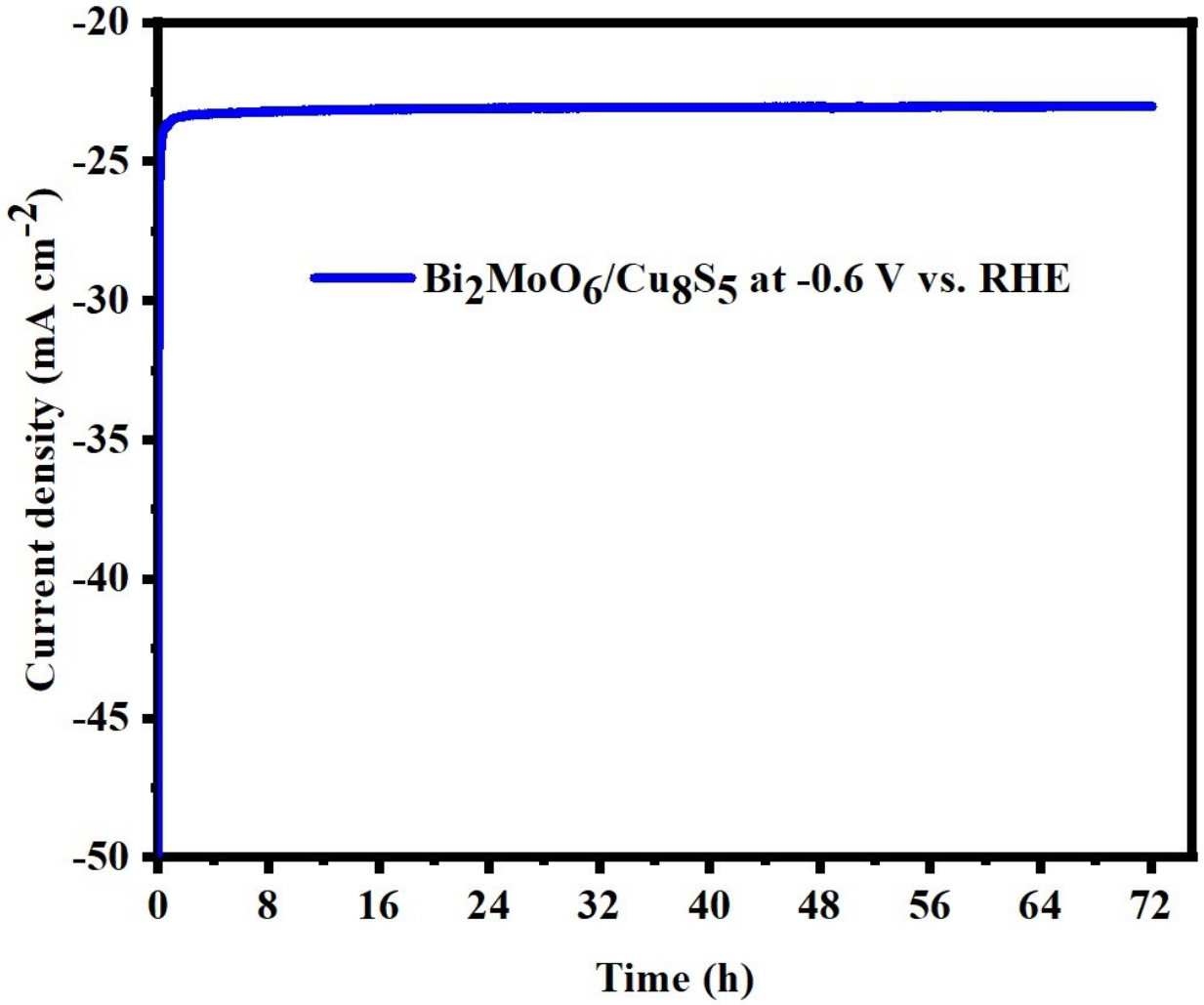

Fig. S15. A 72-hour CA profile of the Bi_2MoO_6/Cu_8S_5 catalyst in electrolyte under N_2 saturation at –0.6 V vs. RHE

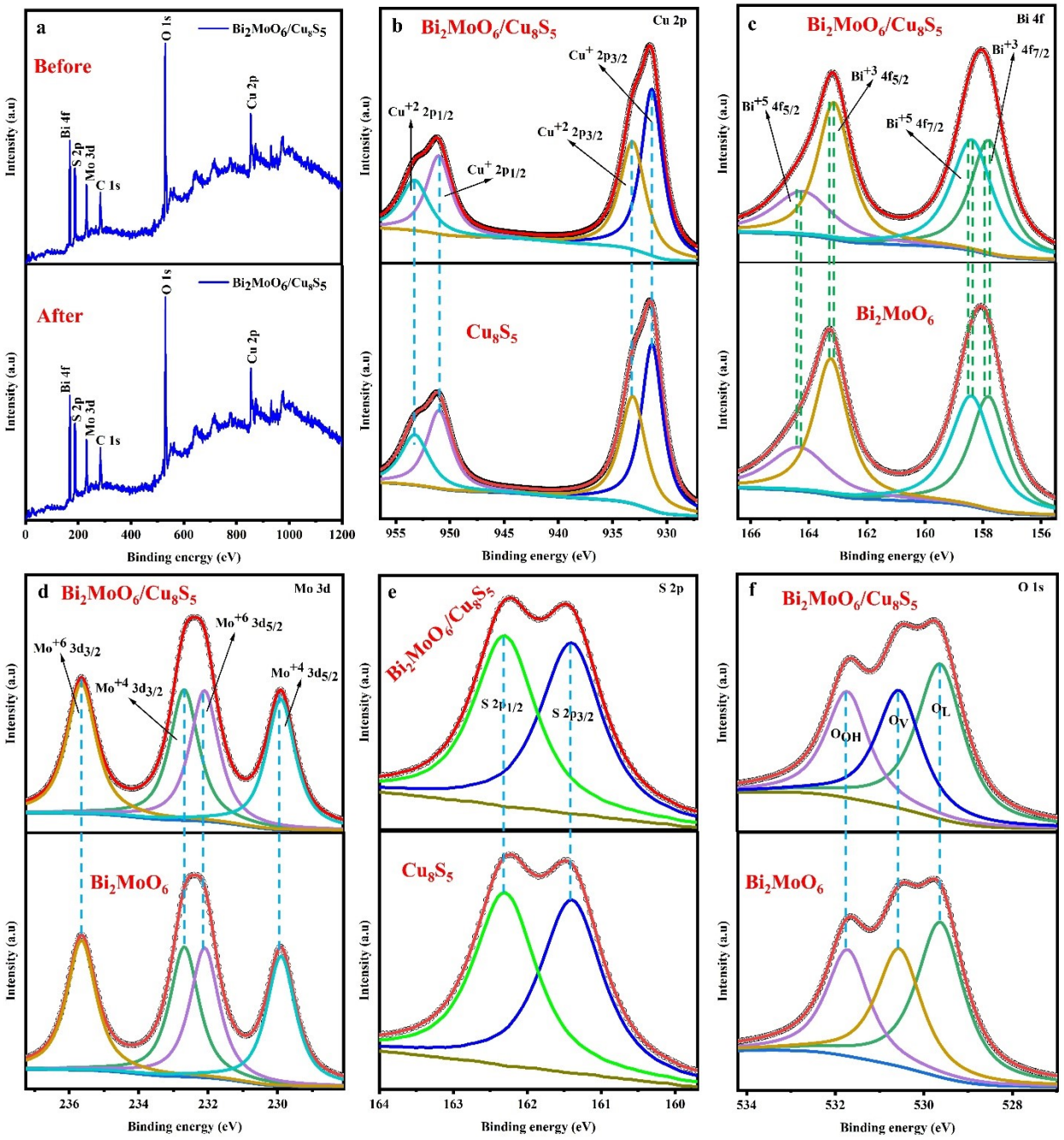

Fig. S16. (a) Full XPS spectra of Bi_2MoO_6/Cu_8S_5 and XPS spectra: (b) Cu 2p, (c) Bi 4f, (d) Mo 3d, (e) S 2p, and (f) O 1s for pure Bi_2MoO_6, Cu_8S_5, and Bi_2MoO_6/Cu_8S_5.

Author contributions

Abera Mitiku Abambagade: Visualization, Methodology, Software, Formal analysis, Investigation, Data curation, Writing – original draft, Conceptualization. **Meselu Eskezia Ayalew:** Visualization, Software, Methodology, Data curation. **Tsegaye Girma Eshetu:** Visualization, Statistical analysis, Investigation. **Quoc-Nam Ha:** Software operation, Technical support, Validation. **Xiaoyun Chen:** Illustration, Technical assistance, Validation. **Mikha Zefanya Silitonga:** Software, Instrument operation. **Van-Nho Tran:** Software, data processing. **Li-Duan Tsai**: Software, Conceptualization, Provided industrial insights. **Yin-Wen Tsai**: Software, Conceptualization, Technical guidance. **Dong-Hau Kuo:** Writing-review & editing, Visualization, Supervision, Validation, Resources, Conceptualization, Project administration.

Conflicts of interest

No conflicts exist to report.

Acknowledgments

This study was supported by the National Science and Technology Council (NSTC), Taiwan, under grant MOST-113-2221-E-011-061-MY3, and partially by the Industrial Technology Research Institute under the 2025-year grant.

SUPPLEMENTARY REFERENCES

1. N. Eprilia, A. R. Sanjaya, R. K. Pramadewandaru, T. A. H. Pertiwi, Y. Putri, I. Rahmawati, B. E. Dewi, Y. K. Krisnandi, H. Chung and T. A. Ivandini, *RSC Adv*, 2024, **14**, 10768-10775.
2. Y. Wang, Z. Ji and Y. Pei, *J Hazard Mater*, 2024, **463**, 132813.
3. R. Qin, Y. Zhang, H. Xu and P. Nie, *ACS Applied Nano Materials*, 2023, **7**, 577-593.
4. A. Assafiri, C. Jia, D. S. Thomas, D. B. Hibbert and C. Zhao, *Small Methods*, 2024, **8**, e2301373.
5. J. Sun, R. Zhou, J. Hong, Y. Gao, Z. Qu, Z. Liu, D. Liu, T. Zhang, R. Zhou, K. Ostrikov, P. Cullen, E. C. Lovell, R. Amal and A. R. Jalili, *Applied Catalysis B: Environmental*, 2024, **342**.
6. S. Bhowmick, A. Adalder, A. Maiti, S. Kapse, R. Thapa, S. Mondal and U. K. Ghorai, *Chem Sci*, 2025, **16**, 4806-4814.
7. D. Ješić, B. Pomeroy, K. M. Kamal, Ž. Kovačič, M. Huš and B. Likozar, *Advanced Energy and Sustainability Research*, 2024, DOI: 10.1002/aesr.202400083.
8. Q. Gao, B. Yao, Y. Liu, L. Shi, Z. Yan, L. Xu, Q. He and H. Zhu, *Chem Catalysis*, 2025, DOI: 10.1016/j.checat.2025.101328.
9. C. V. S. Almeida and L. H. Mascaro, *Electrochimica Acta*, 2024, **476**.
10. A. Shehzad, L. Geng and Z. Luo, *J Phys Chem Lett*, 2025, **16**, 5538-5545.
11. D. Maldonado-Lopez, P. W. Huang, K. R. Sanchez-Lievanos, G. Jana, J. L. Mendoza-Cortes, K. E. Knowles and M. C. Hatzell, *Advanced Functional Materials*, 2024, **35**.